SUBCONTRACT TITLE: **FABRICATION AND PHYSICS OF CDTE DEVICES BY SPUTTERING**

SUBCONTRACT NO: **RXL-5-44205-01**

QUARTERLY TECHNICAL STATUS REPORT FOR:

Phase 2/Quarter 1

SUBMITTED TO: **Bolko von Roedern**
National Renewable Energy Laboratory

PRINCIPAL INVESTIGATORS:

A.D. Compaan (P.I.), V. G. Karpov (co-P.I.), and
R.W. Collins (co-P.I.)
University of Toledo,
Department of Physics and Astronomy,
2801 W Bancroft,
Toledo, OH 43606

This progress report covers the First Quarter of Phase 2 for the period from
June 1, 2006 through August 31, 2006,
of the above Thin Film Photovoltaic Partnership Program subcontract.
The focus of research during this quarter was on materials issues including high rate deposition and in situ real time analysis of film growth and post-processing. In this report recent results of high rate sputter deposition (Task 2.1.3) and real-time spectroscopic ellipsometry study of rf-sputtered solar cells (task 2.3.3) have been described.

Contents

Section 1:   High Rate Sputter Deposition of CdTe (Task 2.1.3)

Section 2:   Real Time Spectroscopic Ellipsometry (Task 2.3.3)

2.1 Nucleation of CdS Films Deposited at Different Temperatures

2.2 Optical Properties of CdS Films Deposited at Different Temperatures

2.3 Co-Sputtering of CdS_xTe_{1-x} Alloys

2.4 Role of $CdCl_2$ Post-Deposition Treatment of CdTe

Section 1: High Rate Sputter Deposition of CdTe (Task 2.1.3)

In our Annual Report for Phase 1 of this Subcontract, we reported that the CdTe film growth rate increases monotonically with decreasing pressure of the sputtering gas in the range of 50 to 5 mTorr, where the rate reaches its maximum. This behavior was associated with an increase of the mean free path with decreasing pressure as long as the pressure remains high enough to sustain a stable discharge. Eventually, when the pressure decreases below 5 mTorr, the rf plasma becomes unstable and the average deposition rate decreases. Thus, the deposition rate is maximum at 5 mTorr where the deposition rate is about 5.5 Å/s at the standard 20 W of RF power applied to the two-inch diameter CdTe target.

In this section, we describe a second phase of studies of the rate dependence primarily aimed at investigating the power dependence of the deposition rate with pressure kept constant. We chose 5 mTorr for the following series of experiments. Note that this study utilized our traditional sputter system with sputter gun directly opposite the vertically oriented substrate as opposed to the work of the previous section which utilized two guns angled toward the substrate which was held horizontally.

All samples were deposited in our RF magnetron sputtering chamber with the magnetron oriented sideways and the substrate vertical. Depositions were performed at 5 mTorr of Ar, with substrate temperature of 250°C. The distance between the 2-inch CdTe target and 3x3 inch square substrate was 6.5 cm. All the samples were standard TEC-7/CdS/CdTe cell structures with CdTe layer thickness of 2.2 ± 0.1 microns. Thickness was controlled in-situ with a He-Ne laser-based transmission monitor and then confirmed by DEKTAK profilometer measurements. RF power was varied in the range of 20 W to 70 W. The deposition rate dependence on rf power is shown in Fig. 1.1.
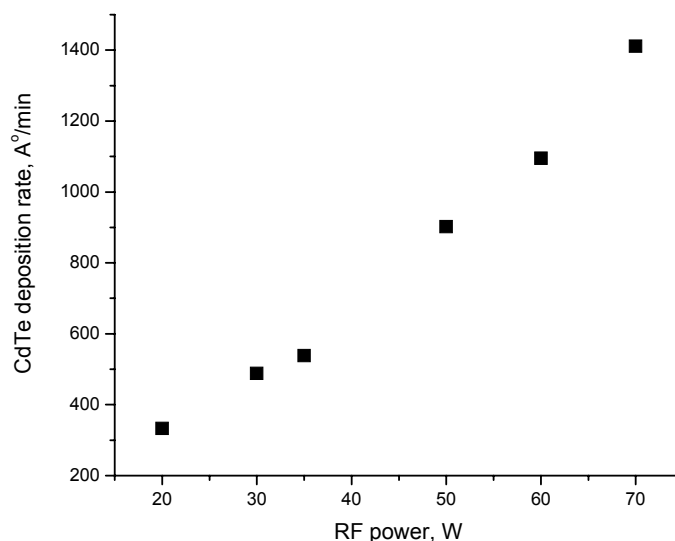
Figure 1.1. *Deposition rate vs. applied RF power at 5 mTorr.*

The deposition rate exhibits a superlinear dependence on power in the range chosen for this study. The lowest point on the graph represents a deposition rate of 335 Å/min so that a time of the order of 70 minutes was needed to deposit a standard 2.3 micron CdTe film. At the highest power point of the graph (70 W) the deposition is completed in less than 17

minutes at a deposition rate of about 1400 Å/min which is more than 5 times faster than our baseline process. Higher powers have not been explored so far since we are using an unbacked, ¼ inch thick CdTe target with no thermally conducting compound at the interface between the target and the sputter cathode. It should be possible to achieve a less than 10-minute deposition time for a two-micron CdTe layer with 100 W applied power.

In order to characterize the structural properties of the film, x-ray diffraction data as well as AFM images were obtained. AFM images did not reveal a substantial dependence of surface grain size or morphology on rf power, although our previous results showed that the grain size clearly decreased if the deposition rate increased due to pressure reduction. This observation of the grain size independence of the rf power is supported by XRD data.

All the films, regardless of the deposition conditions, were found to grow with strongly preferred (111) orientation of the cubic phase. The θ-2θ scans show non-(111) planes increasing dramatically after CdCl$_2$ treatment (Fig. 1.2) as observed in previous work. This indicates substantial grain regrowth of these sputtered films during CdCl$_2$ treatment.
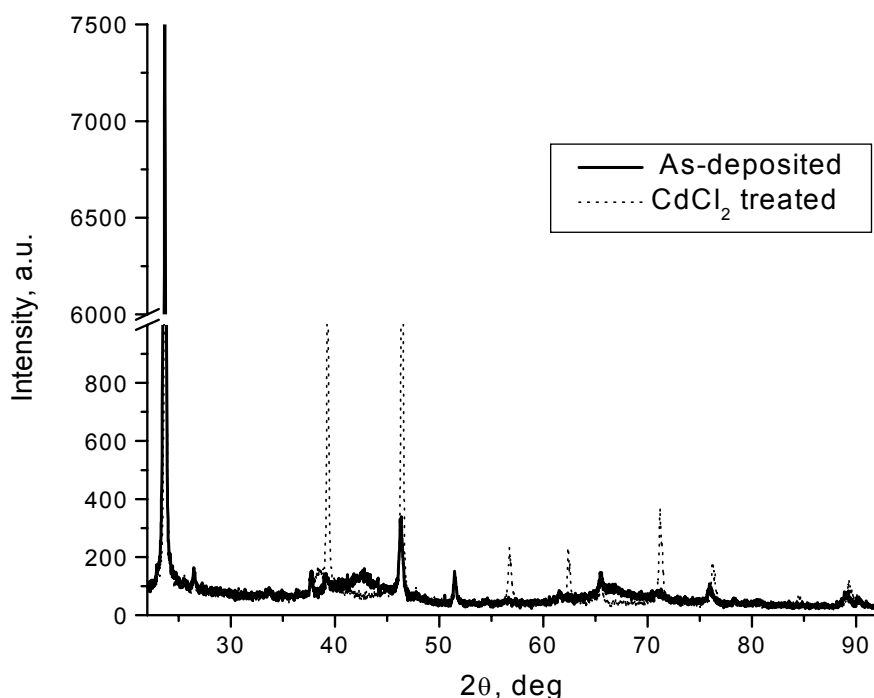

Figure 1.2. *XRD spectra of the cell with CdTe layer deposited at 20W and 5 mTorr before and after CdCl$_2$ treatment.*

Although the XRD diffractograms of as-grown films appear to show little dependence on rf power, a shift of the strongest (111) peak with rf power is observed. The magnitude of the shift varies with the deposition condition. We attribute the peak shifts to residual stress in the films which generally increases with lower pressure and higher rf power. Figures 1.3 and 1.4 emphasize this difference with expanded plots near this peak.
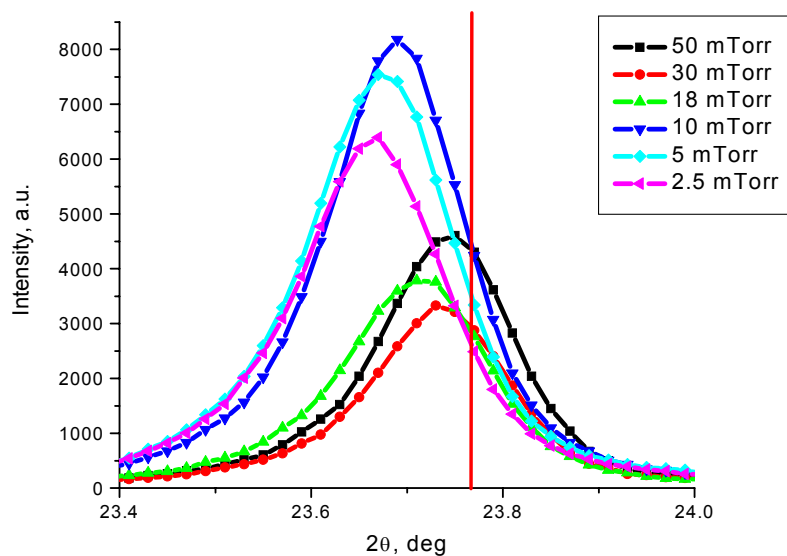
Figure 1.3. *Peak shift of the films grown at constant power of 20 W at variable pressure; the red line represents the position of the peak from a powder sample.*
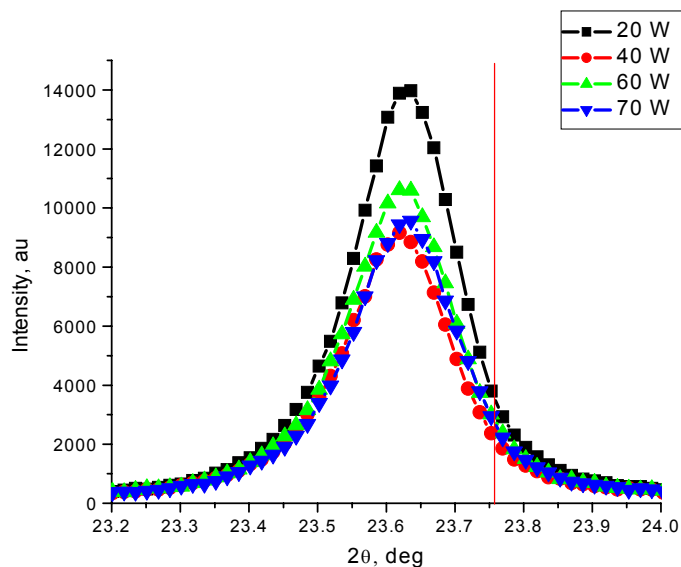

Figure 1.4. *Peak shift of the films grown at constant pressure of 5 mTorr at variable power; red line represents the position of the peak from a powder sample.*

The analysis of the strain extracted from the XRD data of Figures 1.3 and 1.4 shows the trends for the cases of constant 20 W of rf power and variable pressure (Fig. 1.5) and constant pressure of 5 mT and variable rf power (Fig. 1.6).
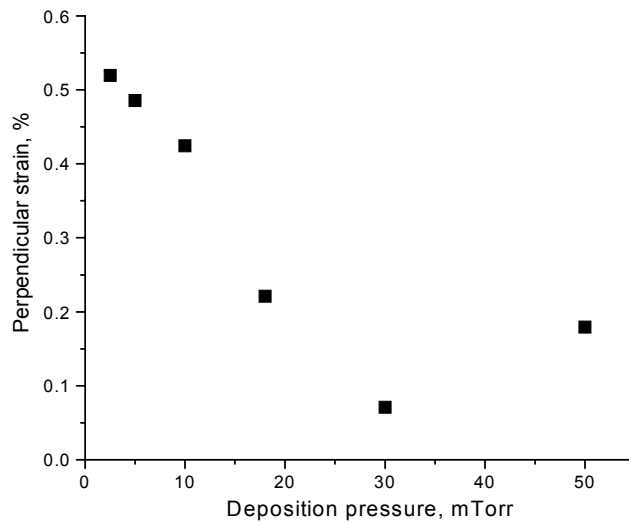
Figure 1.5. Out-of-plane (perpendicular) strain in the films grown at 20 W with pressure from 2.5 mT to 50 mT.
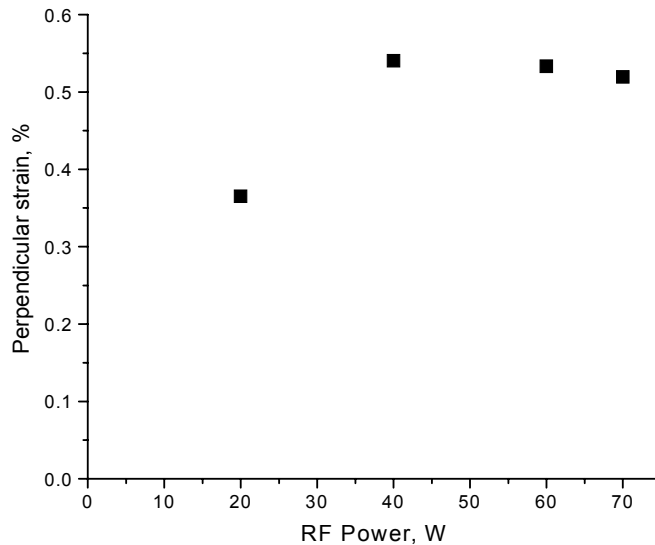

Figure 1.6. Perpendicular strain in the films grown at constant pressure of 5 mTorr at variable power.

There is a strong dependence of residual stress on deposition pressure, but very little strain dependence on rf power. Note that strain (or stress) in the film grown at the highest rates (highest rf power) is little different from that of films grown at lower power. This bodes well for and is consistent with good cell performance observed at high growth rates. (See below.)

A conventional CdCl$_2$ treatment was performed as a part of cell fabrication after the films were grown as described above. We found that our standard CdCl$_2$ conditions work well for releasing the residual stress in all the cells. Figure 1.7 shows the shift of the [111] peak after the CdCl$_2$ treatment for the films grown at 5 and 30 mTorr, when the difference in deposition rates is 1.5 times. In both cases almost complete relaxation is achieved.
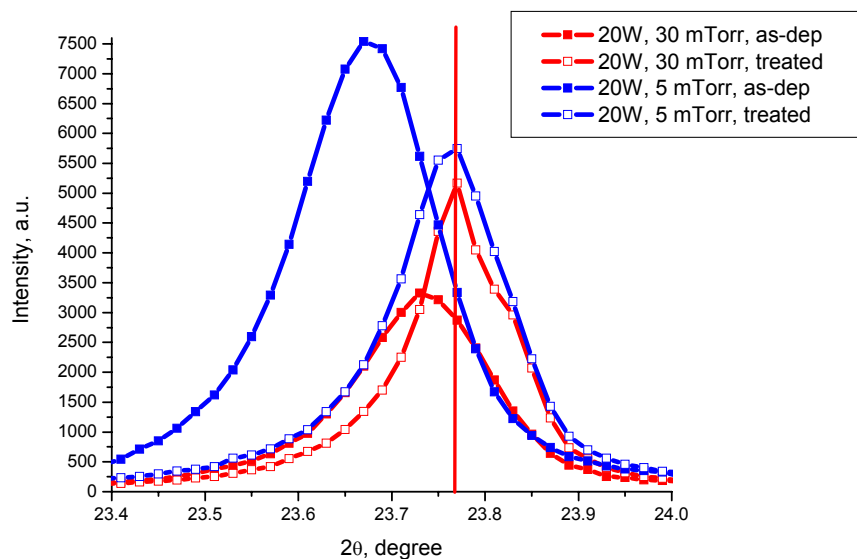

Figure 1.7. *Peak shift after the CdCl$_2$ treatment for the films deposited at different pressures; red line represents the position of the peak from reference sample.*

Finally, solar cells were completed with our standard Cu/Au back contact on the CdCl$_2$ treated films. The highest efficiency achieved was 10.7% for the cell deposited at 1400 Å/min, 9.5% for the cell deposited at 1100 Å/min, and 10.6% for the cell deposited at 900 Å/min. At this point we do not have enough statistical data to justify any meaningful difference in performance between these samples. These results appear to indicate that deposition rate can be increased by almost a factor of five with no meaningful decrease in performance. We are presently focused on further optimization of the chloride process for cells deposited at the higher deposition rates.

Section 2. Real Time Spectroscopic Ellipsometry (Task 2.3.3)

2.1 Nucleation of CdS Films Deposited at Different Temperatures

In previous work presented in the Phase I Annual Report, the nucleation characteristics of 1300 Å thick CdS were described. This section starts with a brief overview of that work and continues with a more detailed description of the recent progress. The series of CdS thin films studied here was deposited on c-Si wafers at different substrate temperatures T over the range from 145°C to 320°C. All other parameters were fixed (rf power = 50 W, Ar pressure = 10 mTorr, Ar flow = 23 sccm).

To begin, one of the key parameters deduced from real time spectroscopic ellipsometry (SE) is the deposition rate. Figure 2.1 compares the deposition rate trend versus substrate temperature for the series of CdS films with a previously-studied series of CdTe films. It is interesting that opposite trends are observed for CdS and CdTe; however, an uncontrolled parameter may exist as noted by the two different rates for the highest temperature CdS depositions. This is likely to be the rf power coupled into the target rather than parameters such as temperature, pressure, or gas flow. The results for CdTe have been corrected for an increase with temperature in the void volume fraction incorporated into the film that leads to an increase in thickness rate at constant atom incorporation rate. As will be shown later, such a correction is not needed for CdS. The possible origin of the increase in rate with temperature for CdTe is a reduction in atom concentration in the gas with increasing gas temperature, but constant pressure. Such a reduction in gas concentration would lead to a reduction in the gas phase scattering of deposited species. Possibly this effect is not dominant in CdS (which shows opposite behavior) due to the lower pressure of CdS deposition (10 mTorr vs. 18 mTorr). The reduction in the deposition rate of CdS with increasing temperature may be due to a reduction in sticking coefficient of the incident growth species with increasing temperature. It is not clear, however, why this is also not a dominant effect in CdTe, as well.

Figure 2.2 shows the nucleation and coalescence characteristics in the first 500 Å of growth for the CdS series. Two clear trends are observed. First, the peak in the roughness evolution which reflects the height of the clusters that form in the nucleation process increases monotonically with increasing temperature. This behavior is attributed to enhanced surface diffusion, resulting in a lower cluster nucleation density during film growth at high temperatures. Second, at the elevated temperatures, the clusters that are larger in size do not completely coalesce and this leads to surface roughness after 100 Å that increases in thickness monotonically with increasing T.   It is interesting that, at the lowest and highest
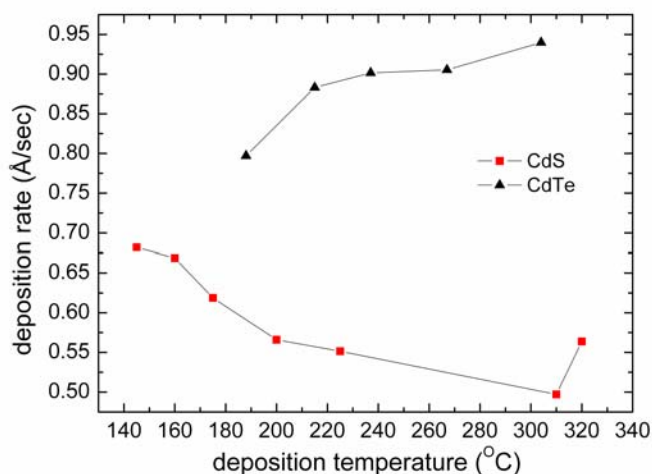
Figure 2.1. *Deposition rate as a function of substrate temperature for the CdS series studied in detail in this report. Corresponding results are also shown for CdTe. For the latter, there is a significant variation in void fraction with substrate temperature that is used to correct the results and extract the true rate which is based on volume of material deposited per unit area. Such a correction is not needed for CdS due to the near constant void volume fraction.*

temperatures, the surface roughness originating from the nucleation process is enhanced with increasing thickness whereas in the intermediate temperature range, 200 - 300°C, the surface roughness is relatively stable. As a result, for the final films (~1300 Å thick), a broad minimum surface roughness thickness of 8-9 Å is observed over this intermediate temperature range. In fact, these CdS films are remarkably smooth for a sputter-deposition process. At the corresponding thickness of 1300 Å, CdTe films, whose nucleation behavior versus substrate temperature was studied earlier, also show a minimum in the surface roughness thickness at the center of this range ~ 240°C, as shown in Fig. 2.3. For CdTe, however, the surface roughness thickness minimum is more clearly defined and the roughness thickness at the minimum, ~ 40 Å, is much larger than that for CdS. In addition, Fig. 2.4 shows the average void volume fraction within the top-most part of the 1300 Å film for CdS in comparison to previous data for CdTe. These results show that CdS can be deposited at near single crystal density throughout the temperature range, whereas for CdTe the single crystal density is obtained only at low substrate temperatures. For CdTe the void fraction increases significantly at higher T.
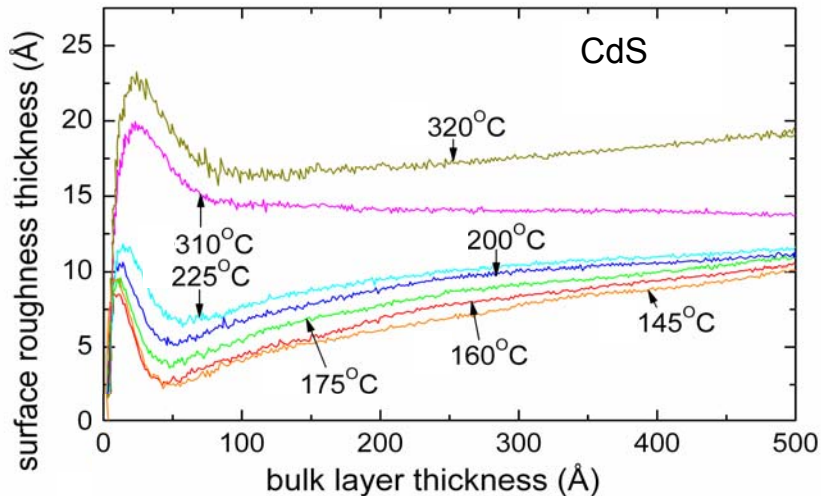

Figure 2.2. *Surface roughness layer thickness versus bulk layer thickness during the initial nucleation and coalescence for CdS films prepared at different deposition temperatures.*
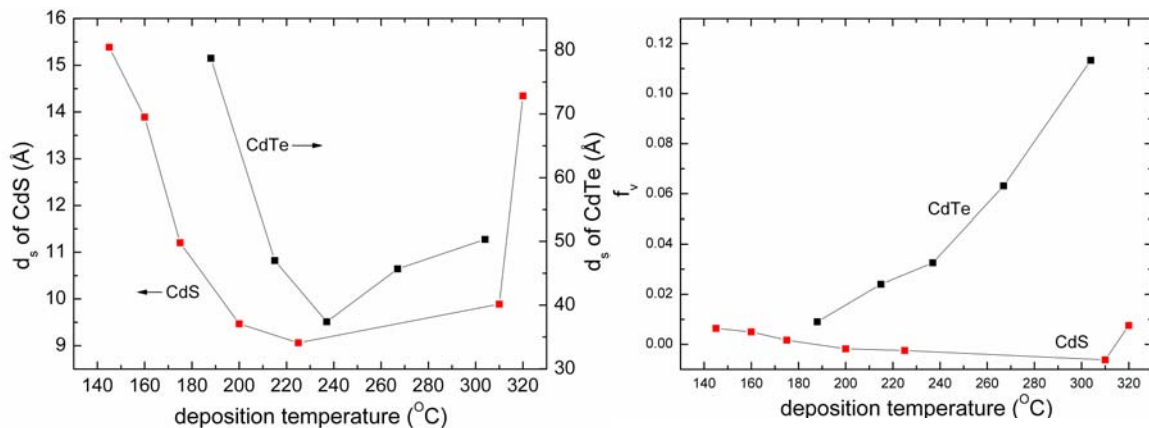

Figure 2.3. (Left) *Surface roughness layer thickness d_s at the end of the deposition for 1300 Å films of CdS plotted vs. substrate temperature. Also shown are results for 1300 Å thick films of CdTe.*
Figure 2.4. (Right) *Relative void volume fraction variations with substrate temperature for the top-most CdTe and CdS after thicknesses of 1300 Å. Void variations with deposition temperature for the CdS are much weaker and exhibit an opposite trend to CdTe.*

New work reported here starts by verifying the validity of the substrate temperature measurement through a more detailed study. Because this is the first study of CdS growth, T was determined from the substrate under vacuum just before plasma ignition. In particular, the red shifts of the E_1 (3.3 eV) and E_2 (4.2 eV) critical points in the optical properties of c-Si relative to their values at room temperature were used to measure T. By analyzing the two critical points, two independent substrate temperature determinations are possible. (Detailed principles can be found in the Phase I Annual Report.) Figure 2.5 shows the Si wafer temperature as a function of thermocouple reading (nominal temperature T_{nom}). The independent measurements are in reasonable agreement. In future studies, the plan is to determine the band gap energy of CdS as a function of true temperature from the calibration of Fig. 2.5. In this way temperature determinations in the future will not rely on a c-Si substrate, and can be obtained from the red shift of the CdS band gap between the deposition temperature (even with the plasma on) and room temperature. In fact, this is the best approach for determining the deposition temperature of the solar cell because the CdS band absorption onset is stronger and even better defined than the CdTe onset and the CdS exhibits greater structural uniformity (smoother surface, low void volume fraction).
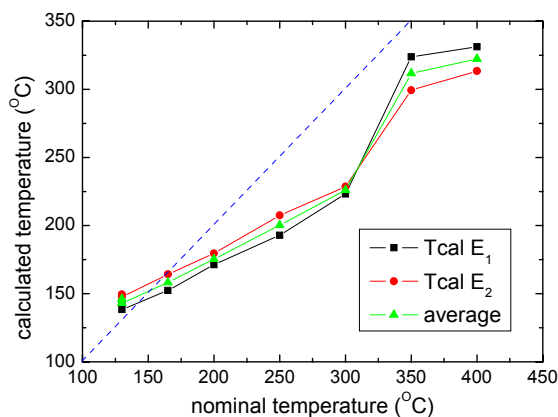

Figure 2.5. *Temperature calculated from the red shifts of the E_1 and E_2 critical points in the optical properties of c-Si as a function of nominal temperature. The red shifts occur between the energies measured from the substrate under vacuum at the deposition temperature just before plasma ignition and the energies measured at room temperature.*

Recent more detailed studies have been focused on the initial nucleation behavior of CdS versus temperature. Figure 2.6 shows the surface roughness evolution in the first 500 Å of film growth as in Fig. 2.2, but highlighting the nucleation behavior by plotting the abscissa on a logarithmic scale. The most important feature observed here is the gradual transition from initial island growth mode (Volmer-Weber mode) at lower temperatures to initial layer-by-layer growth mode followed by islanding (Stranski-Krastanov mode) at higher temperatures. This feature can be observed in Figs. 2.6 and 2.7, the latter showing the surface roughness and bulk layer thicknesses versus time. At the lowest temperature of 145°C, 7 Å of surface roughness develops before the first monolayer (~3 Å) of bulk-density material. In contrast at 225°C, 5 Å of bulk-density material, corresponding to about 1-2 monolayer, forms before the first monolayer of roughness. Similar results to those at 225°C are also obtained at 320°C. The transition from immediate surface roughness (low density film) to immediate bulk (high density film) growth occurs at a temperature of 160°C where both surface roughness and bulk develop essentially simultaneously. This trend with substrate temperature is similar to that of CdTe, however, the corresponding transition for CdTe is 260°C. The observed behavior may indicate enhanced surface diffusion of species on the film surface at higher T that enables more uniform growth and complete filling of the first monolayer.

A key nucleation parameter, the peak surface roughness amplitude just prior to coalescence is plotted in Fig. 2.8. This parameter for the most part exhibits a monotonic trend with deposition temperature, and the fact that the data fit a smooth relationship supports the
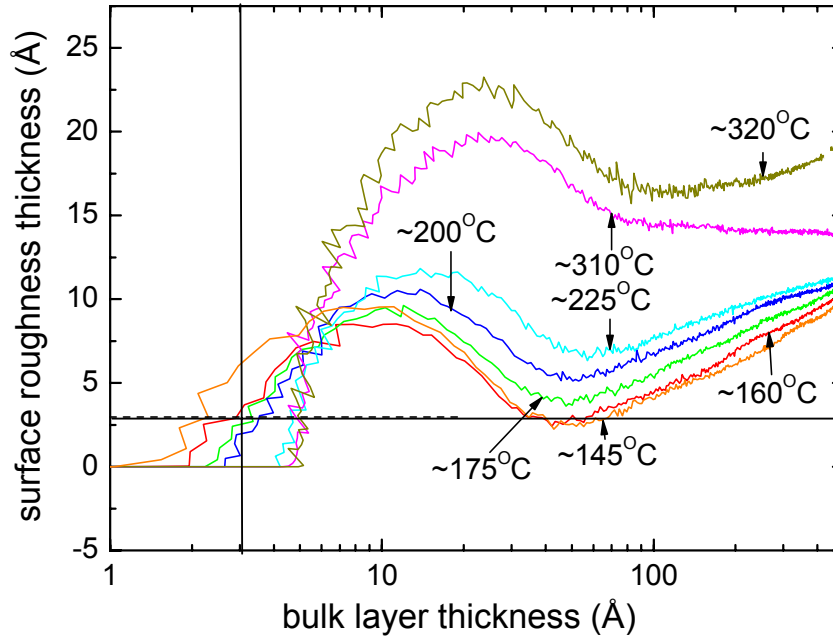
Figure 2.6. *Surface roughness evolution as a function of bulk layer thickness for CdS films deposited at temperatures from 145°C to 320°C. The horizontal and vertical lines indicate surface roughness and bulk layer thicknesses, respectively, of a single monolayer (~3 Å).*
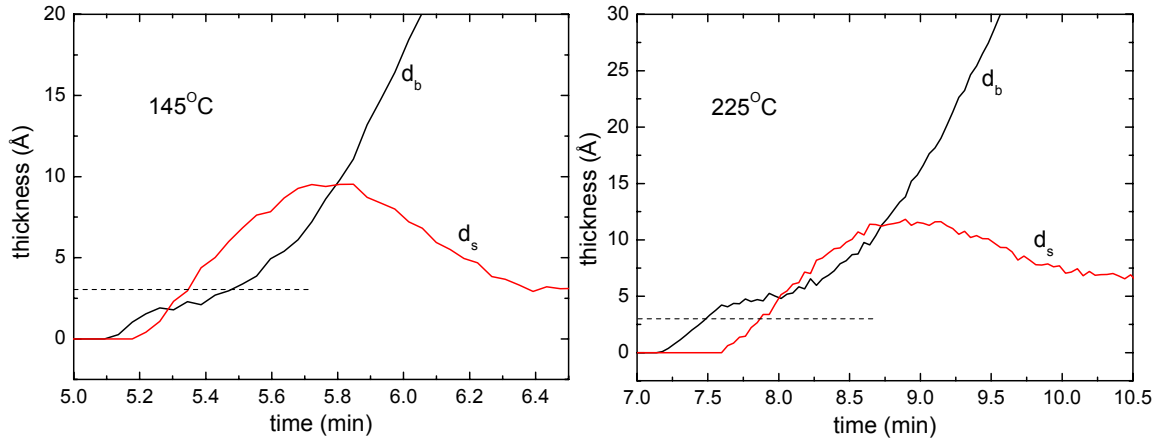

Figure 2.7. *Surface roughness and bulk layer thickness evolution with time. At 145°C **(left)**, after the first two atomic layers of low density surface roughness develop (d_s = 6 Å), the first complete bulk layer has not yet formed (d_b < 3 Å). The situation at this instant consists of a substrate surface partially covered by isolated islands. In contrast, at 225°C **(right)**, almost 2 complete monolayers (5 Å) develop before the first monolayer of surface roughness.*

temperature calibration in spite of the apparent kink at nominal temperatures between 300°C and 350°C. Due to the low peak surface roughness of ~9 Å at low temperature in Fig. 2.8, followed by a coalescence (or smoothening effect) by ~6 Å, a CdS film with a total thickness of 60 Å with an atomically smooth surface (d_s < 3 Å) can be prepared at the lower temperature, providing that the deposition is terminated at the proper time (See Fig. 2.6). This may be very useful for basic material properties studies, such as quantum effects, surface scattering of electrons, interface formation, etc., requiring a very uniform film.
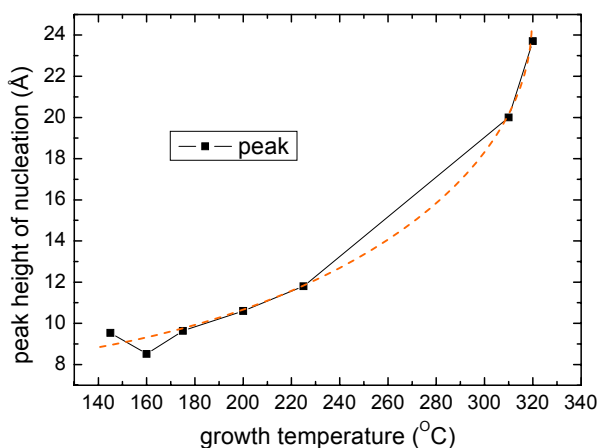
Figure 2.8. *Key nucleation parameter of cluster height for CdS films deposited at different T.*

2.2 Optical Properties of CdS Films Deposited at Different Temperatures

The dielectric functions of the CdS thin films were also extracted after a thickness of 500 Å -- along with the nucleation and structural evolution. At this thickness, the deposition was suspended temporarily and the substrate was cooled for an *in situ* optical measurement at room temperature. Figure 2.9 shows a comparison of the resulting room temperature dielectric functions for the CdS deposited at the lowest and highest substrate temperatures of 145°C and 320°C. Although the optical features for the film deposited at the highest temperature are much sharper, both films reveal an E_1 doublet near 5 eV. SE studies of CdS single crystals reveal that the doublet only occurs in the hexagonal polymorph. The cubic zincblende crystal exhibits a single peak in this energy region near the higher energy peak of the doublet. In addition, Fig. 2.10 shows that the doublet is observed only in the ordinary dielectric function of the hexagonal CdS single crystal. In fact, the E_1 doublet in the dielectric function of the thin film reproduces the shape and relative feature heights of the E_1 doublet in the ordinary dielectric function of the crystal, suggesting that the optical electric field in the thin film measurement is probing the film perpendicular to the optic axis. Accounting for the strong refraction of the incident wave in the CdS, the results suggest that the optic axis is perpendicular to the film surface and thus the film must be highly oriented. Otherwise characteristics of the extraordinary dielectric function of the crystal would be coupled into the thin film data.

To check for consistency with the optical interpretation, x-ray diffraction (XRD) data were collected for the CdS films of the substrate temperature series, as shown in Fig. 2.11. The film thicknesses are all near 1300 Å, accurately determined from the real time SE data. The dominant diffraction peak at $2\theta \sim 26.4°$ appears for both hexagonal close-packed (HCP) and zincblende cubic phases of CdS and thus, cannot be used on its own for CdS crystal structure identification. (All other strong peaks in Fig. 2.11 are due to the c-Si substrate.) The fact that very weak peaks associated with the hexagonal polymorph exist at $2\theta \sim 25°$ and $2\theta \sim 28°$ implies that the film structure as deduced solely by XRD could range from pure hexagonal with strong (002) preferential orientation to oriented zincblende with a small volume fraction of randomly oriented hexagonal phase. Thus in this case, SE can resolve the ambiguity and identifies the correct interpretation as preferentially oriented hexagonal with the optic axis perpendicular to the film surface. For the CdS films deposited at lower T, the two weak features in the XRD -- signs of other hexagonal orientations -- become stronger at the expense of the dominant peak at $2\theta \sim 26.4°$, indicating that the grain orientation is more random at lower T. This effect accompanies an apparent decrease in grain size seen clearly by its effect on the widths of the critical point transitions in the dielectric functions in Fig. 2.9.
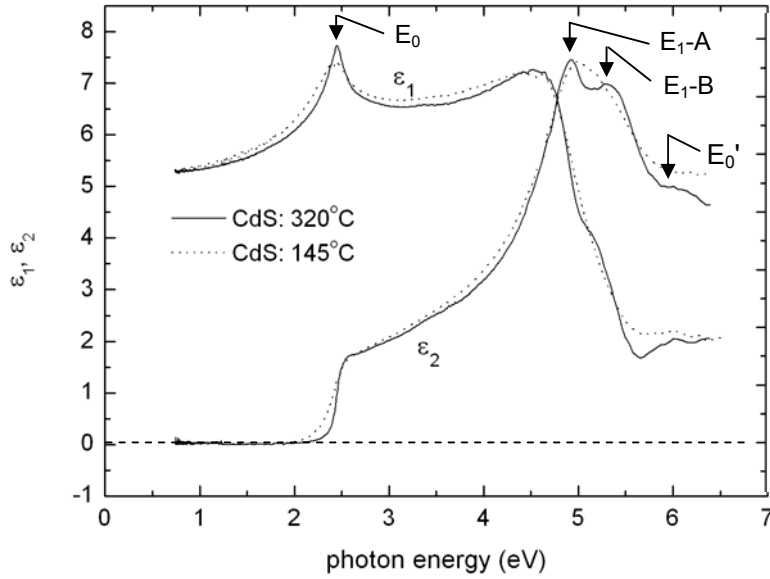
Figure 2.9. *Room temperature dielectric functions of magnetron sputtered CdS films prepared at the lowest (145 ℃) and the highest (320 ℃) substrate temperatures used in this study. The arrows indicate the locations of the E_0 (fundamental band gap), E_1-A, E_1-B, and E_0' critical point energies.*
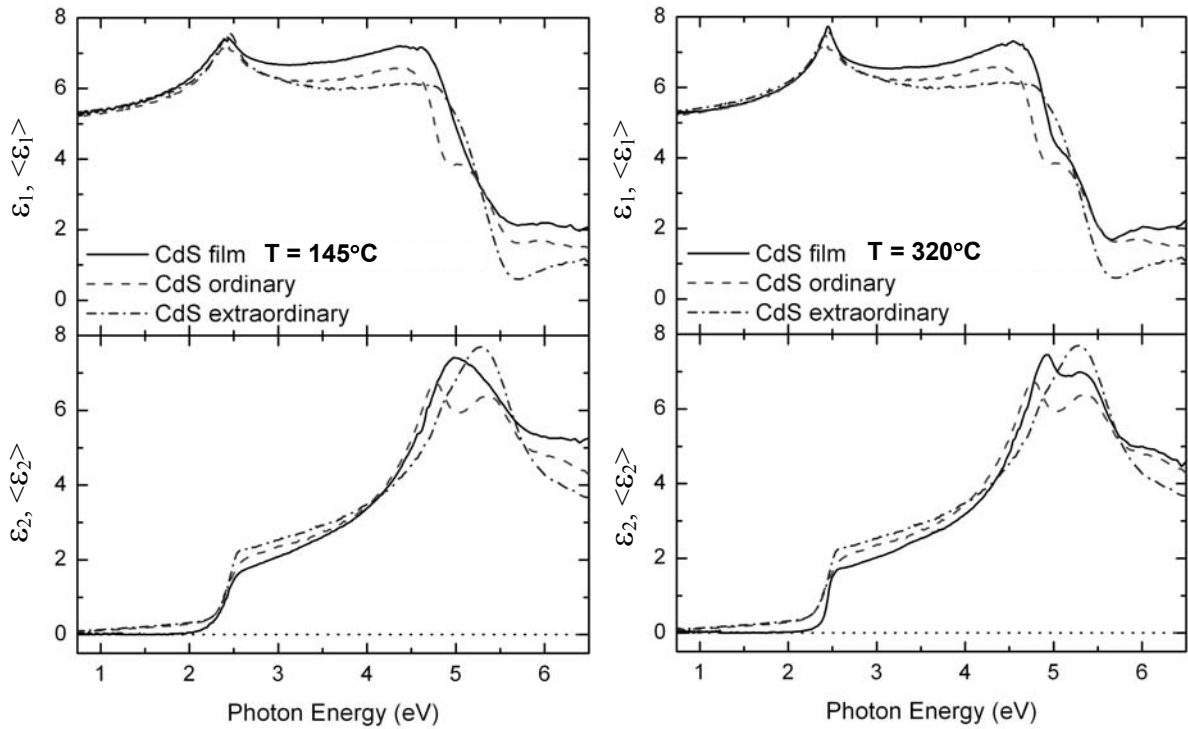

Figure 2.10. *Room temperature dielectric functions ε of magnetron sputtered CdS films prepared at the lowest (145 ℃; left) and the highest (320 ℃; right) substrate temperatures used in this study. Shown for comparison are the ordinary and extra-ordinary wave pseudo-dielectric functions $\langle\varepsilon\rangle$ of the hexagonal form of single crystal CdS. The measurements of the single crystal were performed at University of Toledo using a crystal cut and polished with the c-axis lying in the surface plane. The surface of the crystal was not etched to remove the native oxide; the intact oxide leads to $\langle\varepsilon_2\rangle$ values greater than zero below the gap, and hence the designation pseudo-dielectric functions.*
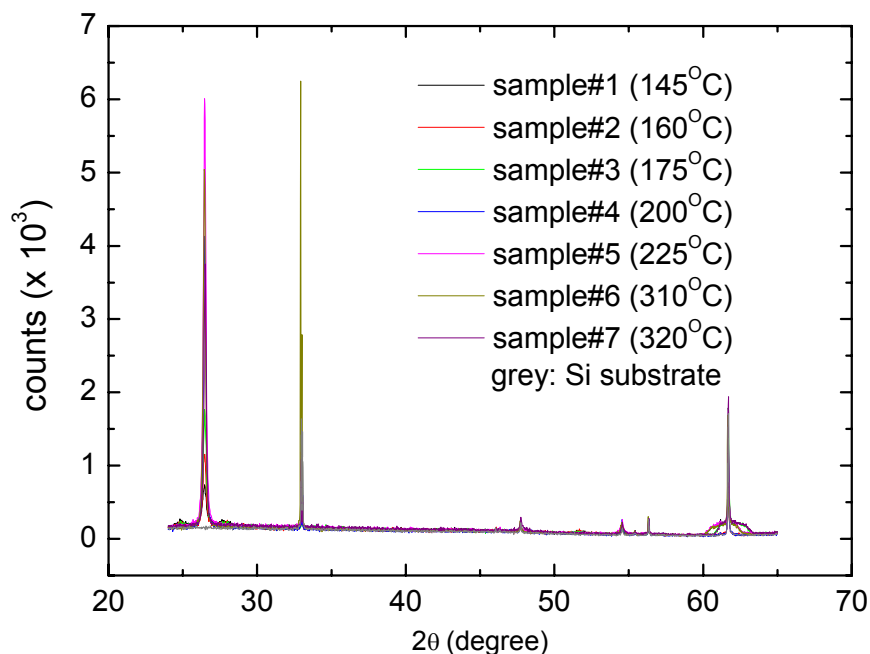
Figure 2.11. *X-ray diffraction data of CdS thin films prepared at different substrate temperatures.*

In particular, a broad band tail can be observed at the band gap transition for the 145°C CdS thin film that is absent for the high temperature film.

In addition to the deposition temperature dependence of the optical properties of CdS, a significant substrate dependence is also possible as shown in Fig. 2.12. This figure depicts four different CdS dielectric functions, two reproduced from Fig. 2.9, a third one obtained in measurements of a sputtered sample deposited onto Corning 7059 borosilicate glass by X. Wu of NREL, and a fourth one deposited onto a vitreous silica prism. For the latter measurement, the optical configuration was different in that the light beam probed the film at the interface to the substrate.

- For the sample prepared at NREL, the lower ε_1 below the band gap, and thus the lower index of refraction, along with the lower amplitude ε_2 structures are attributed to a higher volume fraction of voids relative to the two films prepared on c-Si. In addition, the NREL CdS has a single broad E_1 feature near 5 eV that is shifted toward the higher energy
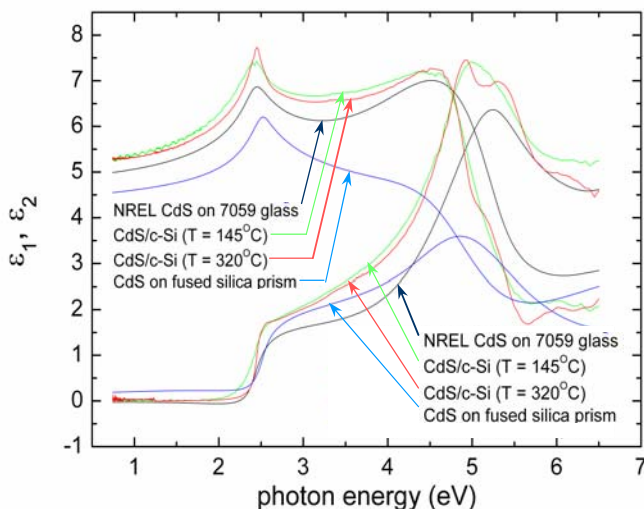

Fig. 2.12. *Dielectric functions of CdS fabricated by sputtering onto c-Si wafer substrates at two temperatures, 145℃ and 320℃, as described in detail in this report. Also shown are the dielectric functions of CdS prepared at NREL onto boro-silicate glass and at University of Toledo onto a vitreous silica prism. In the latter case, the CdS is probed in reflection through the prism.*

peak of the doublet observed for the films on c-Si. Comparison with reference dielectric functions for the single crystal suggest two possibilities. The first possibility is that the single broad feature reflects a hexagonal crystal structure with random polycrystalline orientation. However, because the zincblende polymorph of CdS exhibits a similar E_1 structure as that of the NREL sample of Fig. 2.12, any amount of the zincblende phase in this film is possible. Again a combination of x-ray diffraction and SE may be able to resolve the ambiguity.

- The motivation for studying the CdS film deposited on the vitreous silica prism is to probe the interface to the substrate in reflection through the prism side. It is clear that there is a higher void density for this sample structure than for any of the other samples. The high energy features in ε_1 and ε_2 are strongly suppressed, and this suggests that because the penetration depth of the light is very small (~100 Å) over this photon energy range, the material density is very low at the interface and increases as the bulk of the film is probed. Thus, it is likely that the voids detected in the bulk films on glass and vitreous silica originate from voids generated due to an incomplete coalescence of nuclei in the initial stages of growth. In such cases, some form of processing of the substrate surface may be needed to enhance the nucleation density.

Finally, in order to ascribe the trends in Fig. 2.12 definitively to substrate effects, studies must be performed on CdS films deposited in the same system with the same deposition parameters, but different substrates; such studies are planned for the near future.

2.3 Co-Sputtering of CdS$_x$Te$_{1-x}$ alloys

It is of interest to understand how the CdS and CdTe layers interact during solar cell fabrication. Due to the inter-diffusion at elevated temperatures, it is known that the interaction region can be quite thick and that the alloy composition can vary within the thickness. The optical properties of CdS$_x$Te$_{1-x}$ alloys versus composition and measurement temperature can serve as reference spectra for in situ real time optical characterization of the interaction and junction formation between CdS and CdTe layers. In this study, real time SE has been applied to investigate the initial nucleation, structural evolution, and optical properties of polycrystalline CdS$_x$Te$_{1-x}$ alloy thin films deposited to thicknesses of 200 Å by magnetron co-sputtering of CdTe and CdS targets. A low substrate temperature of T=190°C

The left plot shows the CdTe deposition rate fit:
$$Y = -4.1381 + 0.2629\,X - 0.00441\,X^2 + 3.67681\text{E-}5\,X^3 - 9.05972\text{E-}8\,X^4$$

The right plot shows the CdS deposition rate fit:
$$Y = -2.15516 + 0.15788\,X - 0.00365\,X^2 + 4.20349\text{E-}5\,X^3 - 1.74097\text{E-}7\,X^4$$
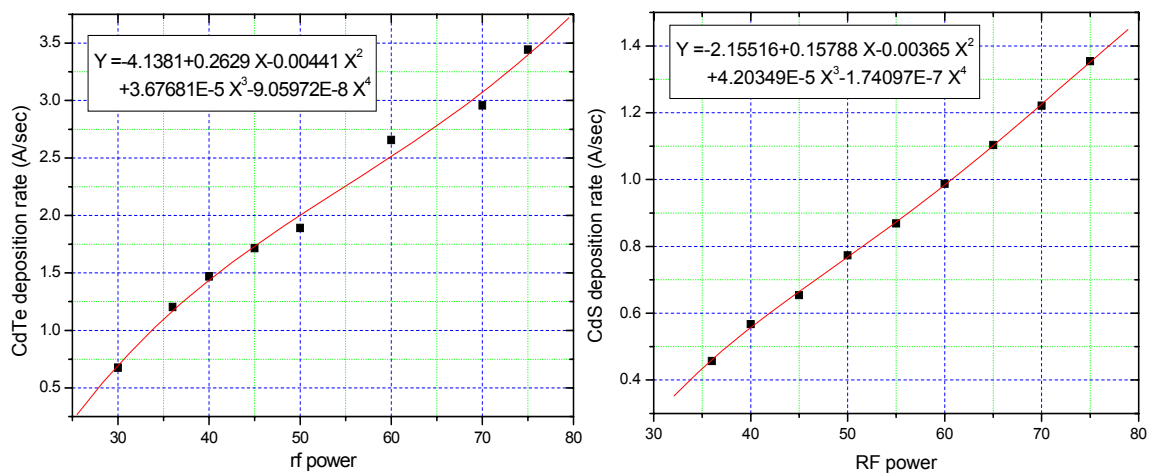
Figure 2.13. *The calibration of CdTe and CdS deposition rates as functions of target RF power. All other deposition parameters are held constant: T = 190°C, Ar pressure = 18 mTorr, and Ar flow = 23 sccm. The solid lines are fourth order polynomial fits to the data that allow one to interpolate the rate from any rf power between the data value extremes and, thus, the molar fraction for any pair of power levels in co-sputtering. For extrapolation, linear fitting of data was performed over restricted ranges.*

Sample #	CdS target power (W)	CdTe target power (W)	x	Sample #	CdS target power (W)	CdTe target power (W)	x
1	0	36	0	13	60	30	0.59
10	33	75	0.10	18	40	25	0.72
11	33	43	0.19	14	60	25	0.82
9	36	36	0.28	15	53	20	0.89
12	35	30	0.39	3	36	0	1

Table 2.1. *Target power levels used in the fabrication of CdS$_x$Te$_{1-x}$ by co-sputtering and the predicted molar fraction of S.*

was used to avoid phase separation. The Ar pressure was 18 mTorr and the flow was 23 sccm. The key variable *x* was determined on the basis of real time SE calibration of the individual CdTe and CdS deposition rates versus target rf power. Figure 2.13 shows the dependence of deposition rate on rf power for the CdTe and CdS targets. The adopted rf powers and the corresponding expected x values are shown in Table 2.1.

The most important data obtained from this study are the optical properties of the alloys as functions of composition as well as measurement temperature. The T = 190°C and T = 17°C dielectric functions are shown in Figs. 2.14 and 2.15, respectively. The general trends observed directly by inspection are as follows: (i) in most cases the dielectric functions vary consistently with x value, and lie between of those of CdTe and CdS --- the two endpoint compositions; (ii) all dielectric functions of the alloys show critical point (CP) features;
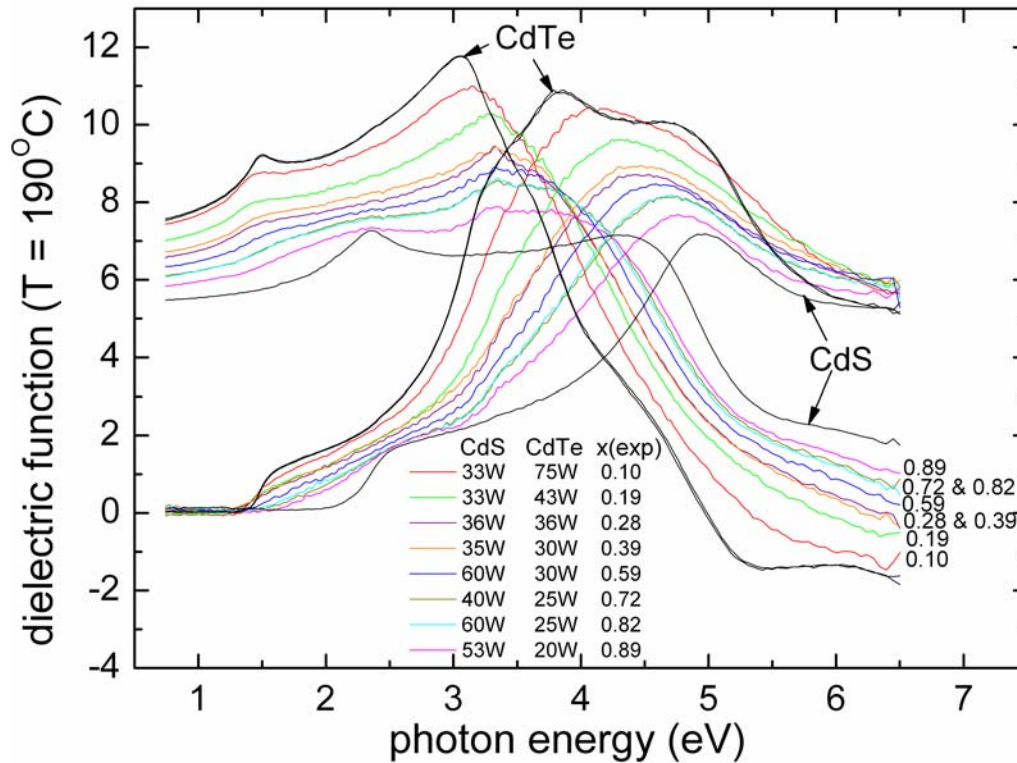

Figure 2.14. *Complex dielectric functions versus x obtained in real time for ~200 Å thick CdS$_x$Te$_{1-x}$ alloys at T = 190°C.*
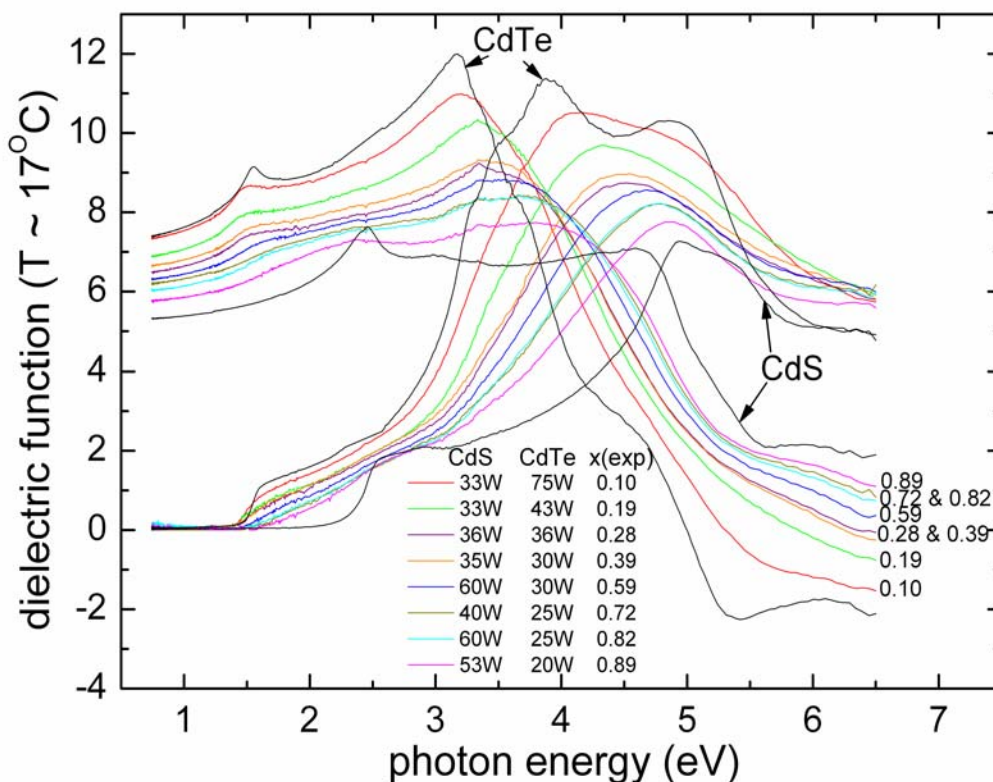
Figure 2.15. *Complex dielectric functions versus x obtained in situ for ~200 Å thick CdS$_x$Te$_{1-x}$ alloys after cooling the deposited film to 17 °C .*

however, these are much broader than the endpoint features; (iii) the apparent band gap shows a clear bowing effect vs. x, observed most clearly in the peak of ε_1, in consistency with previous studies; and (iv) all CP energies, including the band gap, undergo the expected blue shifts when samples are cooled from deposition T to room T.   Similar trends with T have been observed for CdTe and CdS.   Parameterization of these dielectric functions is in progress. Based on this parameterization, one should be able generate the dielectric function of an arbitrary alloy at an arbitrary measurement temperature.
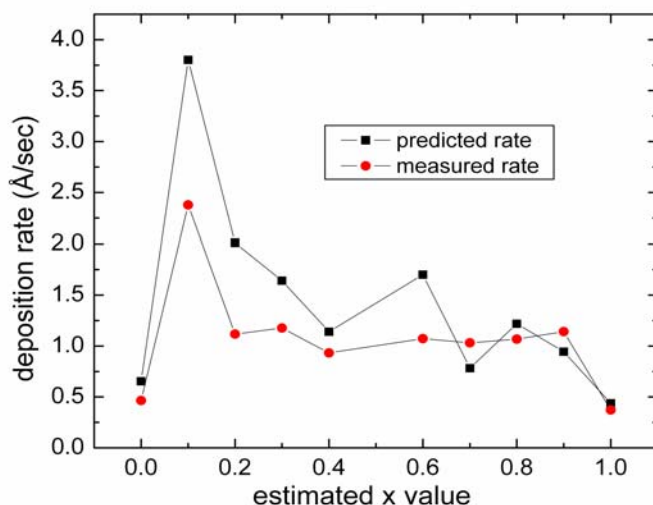

Figure 2.16. *Measured deposition rate versus composition for ~200 Å thick CdS$_x$Te$_{1-x}$ alloys. Also shown are the predicted rates based on the addition of the individual rates from the calibration curves of Fig. 2.13. The difference may be attributed to plasma stabilization on the time scale of minutes and to plasma "crosstalk" at high power levels.*

Turning to the structural evolution of the CdS_xTe_{1-x}, the measured deposition rates are shown versus x in Fig. 2.16. One point to notice is that over a wide range of x from 0.2 to 0.9, the rate is nearly constant, making it easier to relate trends in optical properties and structural evolution to composition over this range, rather than to rate deviations. A problem encountered, however, is highlighted in Fig. 2.16 -- namely that the measured deposition rate for the alloys can be significantly different than the predicted rate based on the calibrations of Fig. 2.13. This effect may be attributed to two possible causes. The first is plasma stabilization on the time scale of 10 min or more during which the rate increases with time at fixed plasma power. This behavior occurs more strongly for the CdTe process than for the CdS process, as indicated by the non-linear calibration curve for the former. The measured rates for the alloys are obtained in the first three minutes after opening the shutter used for presputtering, whereas the calibration data are obtained as a function of time from low to high power over ~40 min. As a result, one can understand why the predicted rate is higher than the measured rate for high CdTe plasma power levels (low x) and lower than the predicted power for low power levels (high x). A second cause of the deviation in Fig. 2.16 may be plasma interference in which case the plasma may expand into the region between the sputter sources when both are operating. Such an effect seems possible based on the observation of slow deposition occurring during presputtering when both sputtering sources are operated -- even with shutters blocking the targets. Such deposition is not observed during presputtering when each source is operated separately. Apparently, the errors in x generated by the two effects give rise to non-monotonic behavior for some samples -- most notably for x = 0.28.

Considering next the nucleation characteristics in Fig. 2.17, all alloys show island growth mode (Volmer-Weber mode) at the beginning of deposition regardless of the x value. In addition, they all have similar surface roughness thickness values, $d_s = 21.5\pm1.5$ Å, when the first bulk layer appears ($d_b = 3$ Å). Up to this point, the film growth pattern is almost the same among all alloys. However, the peak amplitude in the nucleating layer thickness (occurring at bulk layer thicknesses from d_b=10 to 25 Å), the roughness after coalescence, and the roughening rate near the end of deposition vary consistently with x. First, the overall roughness amplitude decreases upon addition of S to CdTe considering the nucleation and coalescence regime. For $CdS_{0.28}Te_{0.72}$, the surface is very smooth and stable for the first 200 Å of bulk layer growth -- considerably smoother than pure CdTe. In contrast, the addition of
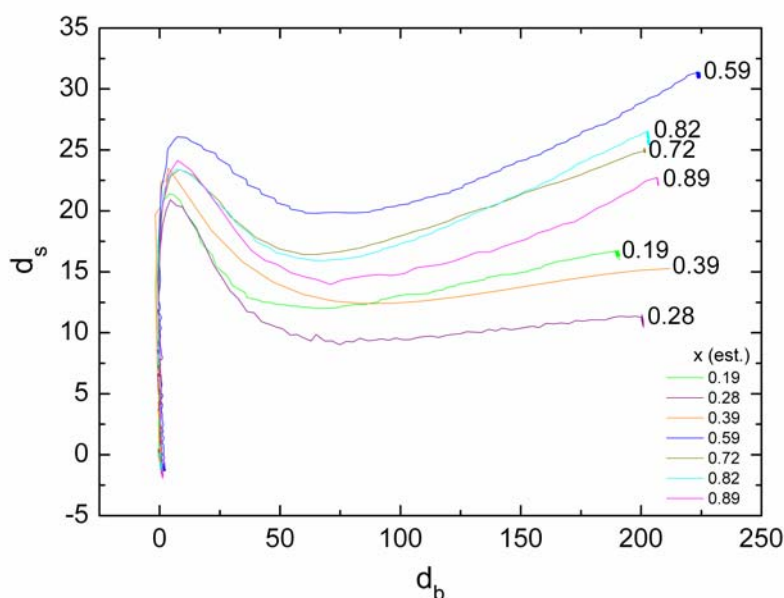

Figure 2.17. Nucleation and surface roughness evolution characteristics of CdS_xTe_{1-x} alloy deposition on c-Si wafer substrates at a deposition temperature of 190 °C. In this plot, d_s is the surface roughness layer thickness and d_b is the bulk layer thickness. The deposition rates of these alloys are similar: 1.05 ± 0.15 Å/s (see Fig. 2.16).

Te to CdS leads to an increase in the roughness amplitude in this regime. For $CdS_{0.59}Te_{0.41}$, the surface is very rough -- considerably rougher than pure CdS even after coalescence, and the roughness is increasing rapidly after 100 Å of bulk layer growth. Because increased surface roughness amplitude has been found to be associated with increased compressive stress as indicated by the blue shift of the band gap relative to the single crystal, then the smoothening with S addition to CdTe is possibly due to the relaxation of compressive stress due to the smaller atomic radius of S relative to Te. Similarly, the enhancement of roughness with addition of Te to CdS may be due to the generation of an additional compressive stress component due to the larger atomic radius of Te. In the composition range between x=0.3 and x=0.6, there is an abrupt transition from the CdTe-rich smooth surface to the CdS-rich rough surface. This increase in roughening between x=0.3 and x=0.6 possibly represents the phase transition from relaxed cubic CdTe to compressively stressed hexagonal CdS.

2.4 Role of CdCl₂ Post-Deposition Treatment of CdTe

Another focus of SE research continues to be the effects of post-deposition processing on the properties of CdTe films deposited by magnetron sputtering on native oxide-covered c-Si substrates. The experiment to be described first applies the etch-back method to ~3000 Å thick CdTe films co-deposited on c-Si substrates held at 188°C. These films were exposed to the following post-deposition processing conditions: (i) as-deposited (i.e., no treatments), (ii) annealed in Ar at 387°C for 30 min, and (iii) CdCl₂ treated also at 387°C, but for 5 min. The new work completed here was to explore the effect of CdCl₂ treatment procedure on the film properties. For each sample prepared here, the etch-back method was performed using successive immersion steps in Br_2+methanol, with each etch step leading to a ~300 Å reduction in the bulk layer thickness. Because of the relative smoothness of the as-deposited CdTe (compared, for example, to depositions on TEC glasses), the successive etching treatments led to very smooth surfaces from which accurate dielectric functions can be determined. In addition, the absence of an underlying CdS film in this case avoids potential complication of alloying of CdTe due to S in-diffusion.

Figure 2.18 presents an overview of previous work in which depth profiles in the E_1 critical point energy and width relative to those of the single crystal provide information on the depth profiles in the strain and grain size, respectively, throughout the film. Similarly, Fig. 2.19 presents depth profiles in the void fraction that provide information on the structural uniformity.

- For the *as-deposited film*, the red-shift of E_1 relative to the single crystal value in the top panel of Figure 2.18 reveals significant strain in this film over the studied depth range of 1500-2000 Å; (the depth is measured relative to the substrate interface at 0 Å). The depth profile in Fig. 2.19 provides additional indirect evidence for this strain; the film is observed to undergo a structural transition near 1500 Å whereby the strain is ultimately relaxed (after 2000 Å thickness) through generation of voids and their continued evolution with thickness. The lower panel shows that the as-deposited film has a very large broadening parameter Γ_{E1} ~ 0.6 ± 0.15 eV, indicative of a very small grain size.

- Upon *Ar annealing of the film*, the strain nearest the substrate is significantly reduced as the grain size increases (reduced Γ_{E1}). Even after 30 min of annealing in Ar, however, there is no significant reduction in the grain size within 500 Å of the surface, and the strain in this region increases somewhat relative to the as-deposited film. Figure 2.19 shows that the void fraction in the surface region is reduced upon annealing in Ar and thus, the structure of the film becomes more uniform throughout the thickness.

- It is interesting that a *5 min CdCl₂ treatment* leads to an E_1 energy within 10 meV of the single crystal value throughout the thickness, suggesting a fully strain-relaxed film. In
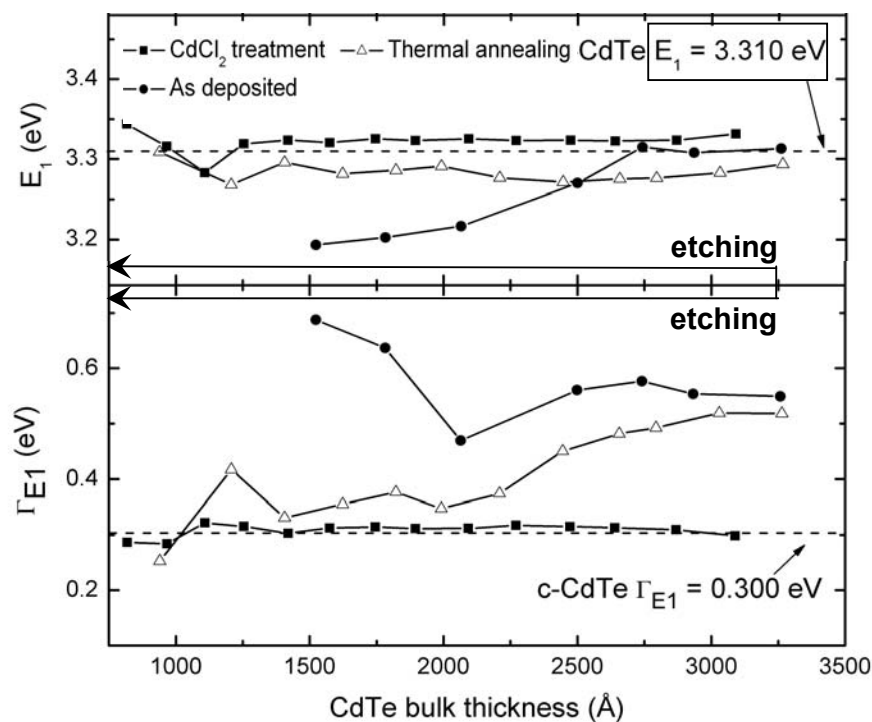
Figure 2.18. *E_1 critical point energies (upper panel) and widths (lower panel) as functions of CdTe bulk layer thickness during etching by Br_2+methanol for co-deposited CdTe films processed in three different ways: (i) as-deposited, (ii) annealed in Ar for 30 min, and (iii) $CdCl_2$ treated for 5 min. The deviations at low thickness are due to the onset of semi-transparency for the critical point energy.*
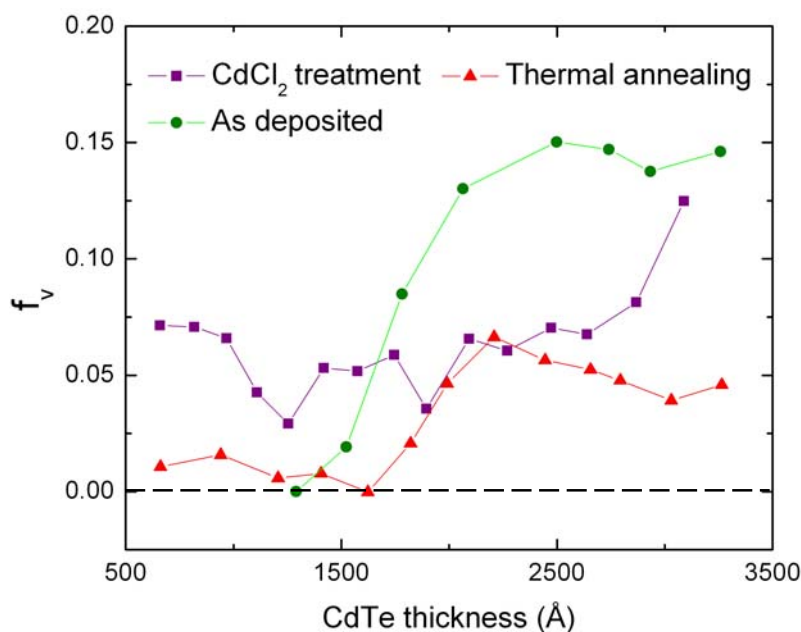

Figure 2.19. *Relative void volume fractions as functions of CdTe bulk layer thickness during etching by Br_2+methanol for co-deposited CdTe films processed in three different ways: (i) as-deposited, (ii) thermally annealed for 30 min, and (iii) $CdCl_2$-treated for 5 min. For the as deposited and annealed films, the void fraction is scaled relative to the depth at which the highest density is observed. For the $CdCl_2$-treated film, the void volume fraction is scaled relative to single crystal CdTe.*

addition, Γ_{E1} has been reduced significantly to a constant value of $\Gamma_{E1} \sim 0.30 \pm 0.02$ eV throughout the bulk of the film, indicating a significant increase in grain size. Finally the $CdCl_2$ treatment leads to a uniform void volume fraction throughout most of the bulk of the film: 0.05 ± 0.025, however, considerable scatter exist in the data, possibly an effect of the Br_2+methanol etching of a large grained film. Figure 2.19 shows that voids have been pushed to the near-surface region of the $CdCl_2$ treated film which is likely to be the result of a larger surface roughness layer thickness..

Results of similar studies of solar cell structures on TEC-15 glass are shown in Figs. 2.20 and 2.21. The solar cells are complete, including $CdCl_2$ treatment, but with the exception of the back contact, and the SE measurements are performed from the film side during etch back. Figure 2.20 shows that the E_1 energy of the CdTe layer remains within ± 5 meV of the single crystal value from 1000 Å to 1.8 μm, indicating stress relaxation throughout the thickness. The results in Fig. 2.21 for the E_1 critical point width Γ_{E1} reveal two important points. First because the value $\Gamma_{E1} \sim 0.26 \pm 0.01$ eV at the film surface side is less than that of single crystal CdTe, it suggests more careful measurements of the single crystal are needed. It is likely that surface scattering in the single crystal is the origin of the larger Γ_{E1} value. Second, the gradual increase in Γ_{E1} as the interface to the CdS is approached indicates that the grain size is decreasing toward this interface and that the grain structure in the cell is not as uniform as for the thin films on c-Si.
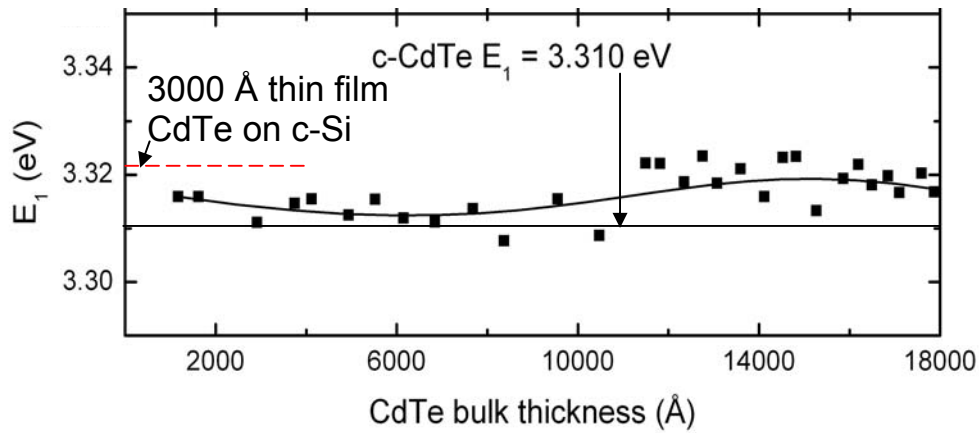

Figure 2.20. *Energy of the E_1 transition as a function of CdTe bulk layer thickness in successive Br_2-methanol etching steps for a sputtered CdTe solar cell. Also shown is the constant energy of the E_1 transition of thin film CdTe (3300 Å thick) fabricated on a c-Si wafer substrate.*
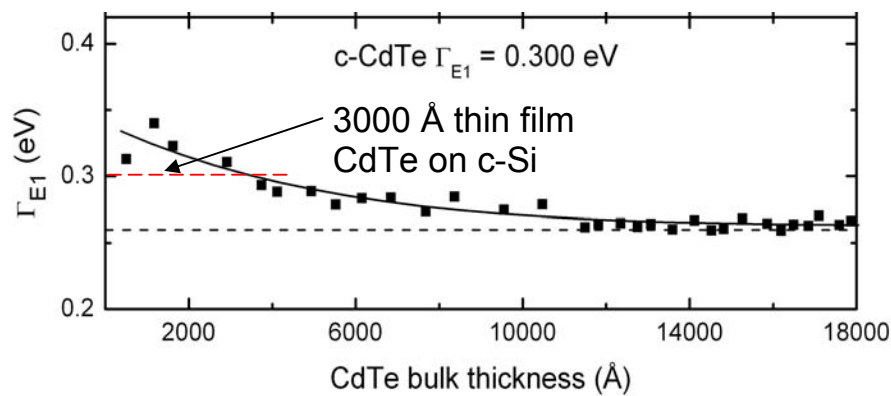

Figure 2.21. *Broadening parameter Γ_{E1} as a function of CdTe bulk layer thickness in successive Br_2-methanol etching steps for a sputtered CdTe solar cell. Also shown is the constant width of the E_1 transition of thin film CdTe (3300 Å thick) fabricated on a c-Si wafer substrate.*
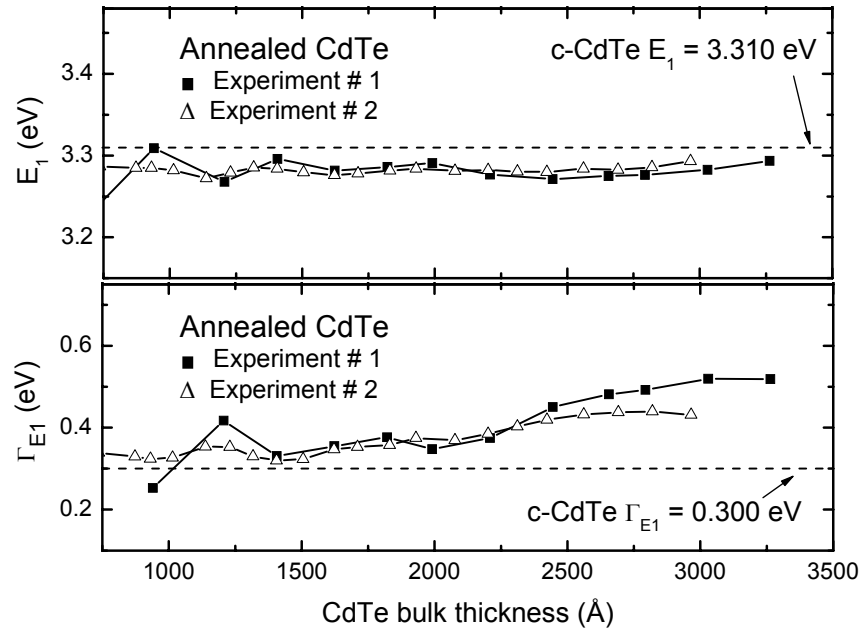
Figure 2.22. *Energy of the E_1 transition (upper panel) and its width Γ_{E1} (lower panel) as functions of CdTe bulk layer thickness in successive Br_2-methanol etching steps for ~3000 Å thick CdTe films. The two films were processed under identical conditions including fabrication on c-Si wafer substrates and anneals in Ar at 387°C for 30 minutes. The data for experiment #1 is the same as those depicted in Fig. 2.18.*
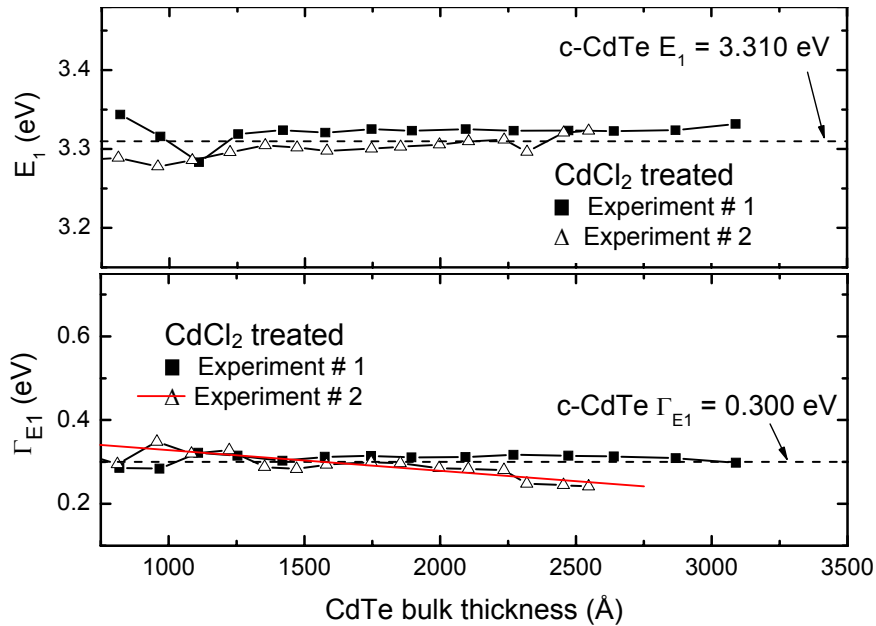

Figure 2.23. *Energy of the E_1 transition (upper panel) and its width Γ_{E1} (lower panel) as functions of CdTe bulk layer thickness in successive Br_2-methanol etching steps for ~3000 Å thick CdTe films. The two films were processed under similar conditions including fabrication on c-Si wafer substrates and $CdCl_2$ treatments for 5 minutes. The data for experiment #1 is the same as those depicted in Fig. 2.18.*

The reproducibility of the etch-back studies of films annealed in Ar has been explored, and the effect of the $CdCl_2$ treatment condition on film structure has also been investigated.

Figure 2.22 shows the Ar annealing behavior of thin (3000-3300 Å) CdTe films on c-Si substrates from two separate experiments for comparison. The solid squares are the same results as shown in Fig. 2.18, and the open triangles are the results of a second experiment performed on a different sample prepared and annealed under identical conditions. The annealing behavior is reasonably well reproduced in the two experiments, considering that the film thickness in the second experiment is somewhat less. In both experiments, the E_1 energy lies ~ 15 meV lower than that of single crystal CdTe, indicating residual strain, and the width Γ_{E1} increases toward the surface, indicating a smaller near-surface grain size in both experiments.

Figure 2.23 shows results for E_1 and Γ_{E1} from two experiments applying $CdCl_2$ treatments for 5 min. The results of the first experiment have been presented earlier in Fig. 2.18. This first experiment was performed with a $CdCl_2$ treatment temperature of 387°C, whereas the second was performed using a higher temperature of 397°C. Another difference between the two experiments -- the age of the prepared $CdCl_2$ sources -- was deemed insignificant. More importantly, for both experiments, the treatment was the starting one for each of the two sources. Although the overall results of the two experiments are similar, certain details in the second experiment appear to reveal the effect of the higher temperature. First, for the second experiment, the grain size increases more significantly toward the surface than in the first experiment. In addition, a comparison of Fig. 2.24 with Fig. 2.19 shows that the void profile in the second experiment is not nearly as uniform as in the first. This feature is likely due the higher temperature which leads to a densification of the underlying large grain crystalline material at the expense of significant roughness that extends well into the film. A hint of this effect appears for the $CdCl_2$ treated film in Fig. 2.19, but the effect appears quite strongly in Fig. 2.24. In the future, complete studies of the effect of $CdCl_2$ treatment time and temperature will be undertaken.
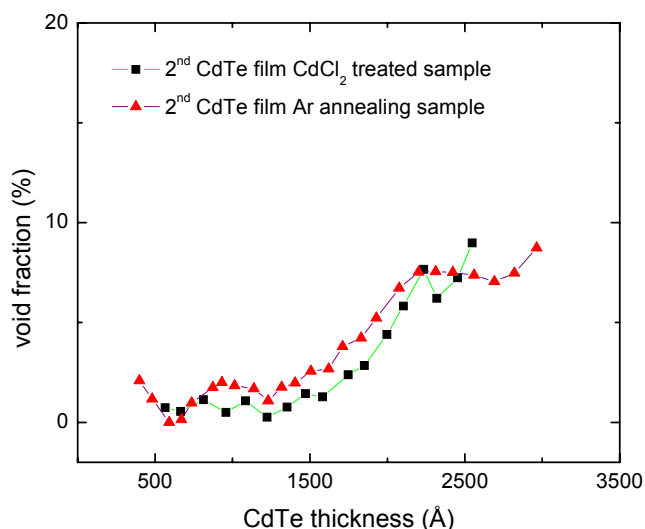

Figure 2.24. *Void volume fraction as a function of CdTe bulk layer thickness in successive Br₂-methanol etching steps for ~3000 Å thick CdTe films in a second experiment for comparison with the results in Fig. 2.19. Two different post-deposition processing procedures were used: (i) anneal in Ar for 30 min, and (ii) CdCl₂-treatment for 5 min. For the Ar annealed films, the void fraction is scaled relative to the depth at which the highest density is observed. For the CdCl₂-treated film, the void volume fraction is scaled relative to single crystal CdTe. The void structure for the film annealed in Ar is attributed to structure in the as-deposited film (as in Fig. 2.19). In contrast, the void structure for the CdCl₂ treated film is attributed to extensive near-surface roughness.*